Inorganic Chemistry

Article

pubs.acs.org/IC

Tetrabenzoporphyrin and -mono-, -*cis*-di- and Tetrabenzotriazaporphyrin Derivatives: Electrochemical and Spectroscopic Implications of meso CH Group Replacement with Nitrogen

Adele van As,[†] Chris C. Joubert,[†] Blenerhassitt E. Buitendach,[†] Elizabeth Erasmus,[†] Jeanet Conradie,[†] Andrew N. Cammidge,[‡] Isabelle Chambrier,[‡] Michael J. Cook,[‡] and Jannie C. Swarts*[,†]

[†]Department of Chemistry, University of the Free State, Bloemfontein 9300, South Africa

[‡]School of Chemistry, University of East Anglia, Norwich NR4 7TJ, United Kingdom

Supporting Information

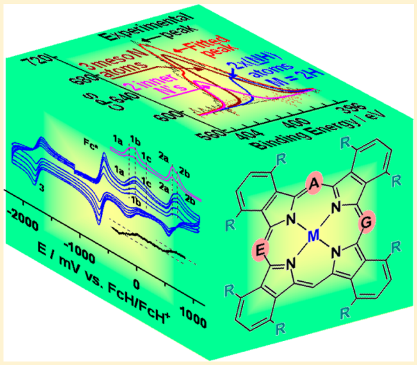

ABSTRACT: Nonperipherally hexyl-substituted metal-free tetrabenzoporphyrin (2H-TBP, **1a**) tetrabenzomonoazaporphyrin (2H-TBMAP, **2a**), tetrabenzo-*cis*-diazaporphyrin (2H-TBDAP, **3a**), tetrabenzotriazaporphyrin (2H-TBTAP, **4a**), and phthalocyanine (2H-Pc, **5a**), as well as their copper complexes (**1b**−**5b**), were synthesized. As the number of meso nitrogen atoms increases from zero to four, λ_{max} of the Q-band absorption peak becomes red-shifted by almost 100 nm, and extinction coefficients increased at least threefold. Simultaneously the blue-shifted Soret (UV) band substantially decreased in intensity. These changes were related to the relative electron-density of each macrocycle expressed as the group electronegativity sum of all meso N and CH atom groups, $\sum\chi_R$. X-ray photoelectron spectroscopy differentiated between the three different types of macrocyclic nitrogen atoms (the N_{inner}, $(\underline{N}H)_{inner}$, and N_{meso}) in the metal-free complexes. Binding energies of the N_{meso} and $N_{inner,Cu}$ atoms in copper chelates could not be resolved. Copper insertion lowered especially the cathodic redox potentials, while all four observed redox processes occurred at larger potentials as the number of meso nitrogens increased. Computational chemical methods using density functional theory confirmed **1b** to exhibit a Cu(II) reduction prior to ring-based reductions, while for **2b**, Cu(II) reduction is the first reductive step only if the nonperipheral substituents are hydrogen. When they are methyl groups, it is the second reduction process; when they are ethyl, propyl, or hexyl, it becomes the third reductive process. Spectro-electrochemical measurements showed redox processes were associated with a substantial change in intensity of at least two main absorbances (the Q and Soret bands) in the UV spectra of these compounds.

1. INTRODUCTION

Phthalocyanines (Pcs) belong to a man-made class of macrocyclic compounds[1] that have found widespread applications as industrial catalysts,[2] commercial colorants,[3] and functional materials for applications in areas as diverse as optical data storage,[4] electrophotography,[5] gas sensing,[6] and the photodynamic therapy of cancer.[7] They also exhibit potential for exploitation in the development of technologies requiring liquid crystals,[8] memory devices,[9] optical limiting,[10] and water purification.[11] Appropriate substituents on the phthalocyanine ring system confer solubility in either aqueous or organic solvents onto the otherwise essentially insoluble macrocyclic core.[12] The electrochemistry of phthalocyanines often offers two, mostly electrochemical reversible, ring-based reductive couples and two ring-based oxidative couples in CH_2Cl_2 as solvent, although in the case of, for example, zirconium and hafnium phthalocyanines, more reductive steps have been observed.[13] In other solvents, sometimes three or four ring-based reductions may be observed.[14,15]

In contrast, porphyrins are naturally occurring macrocycles of similar structure but of lower stability than phthalocyanines; they are especially well-known as oxygen carriers[16] and electron-transfer mediators[17] in biological processes, and the mode of axial ligation in oxygen-carrying porphyrins has been the focus of computational studies.[18] They can also be used as catalysts[19] and in photodynamic cancer therapy.[20] The porphyrin macrocyclic core differs in structure from that of a phthalocyanine at the macrocyclic apexes (meso positions) having four CH or CR groups, while phthalocyanines have four nitrogens, and in phthalocyanines a benzene ring is annulated to the pyrrole fragments of the macrocyclic rings, Figure 1.

These structural differences induce different electrochemical and spectroscopic properties in the two macrocyclic subclasses. Although porphyrins also exhibit four ring-based redox processes in CH_2Cl_2, the redox potentials at which reduction takes place in metal-free and nickel or zinc porphyrins[21] are

Received: February 16, 2015
Published: May 13, 2015

DOI: 10.1021/acs.inorgchem.5b00380
Inorg. Chem. 2015, 54, 5329−5341

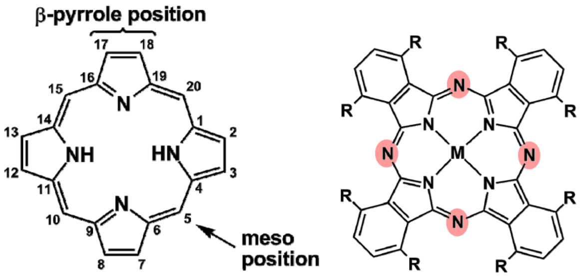

Figure 1. Porphyrin (left) and a nonperipherally substituted phthalocyanine (right). R = large groups, such as hexyl in this work, to enhance solubility in organic solvents. M can be any of more than 70 elements, but here M = 2H or Cu. Key structural differences between porphyrins and phthalocyanines are the four nitrogen atoms at the apexes of the phthalocyanine macrocycle (meso positions in porphyrins) as well as the annulated benzene rings to the pyrrolic fragments.

Scheme 1. Synthesis of Metal-Free and Copper-Coordinated Hybrid Benzoporphyrins Bearing Monoaza, Diaza, and Triaza Apexes (Nitrogen Meso Atoms)[a]

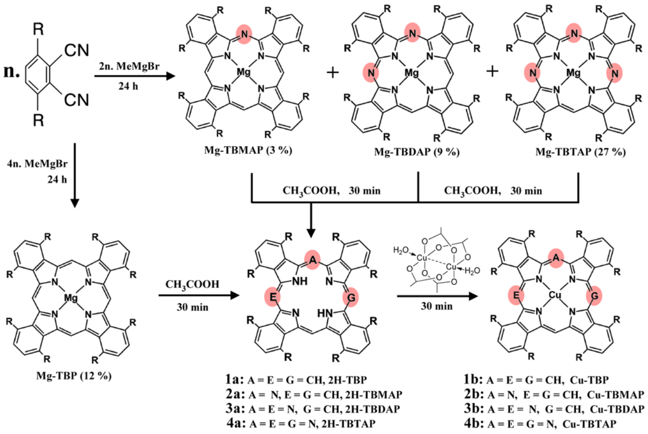

[a]R = hexyl, and notations used for these compounds in the text.

frequently up to 500 mV smaller than those for phthalocyanines,[13a] while the two porphyrin oxidative redox steps[21] may occur at potentials 200 mV larger than for phthalocyanines.[13a] Spectroscopically, the major porphyrin electronic absorptions include the Soret band at ca. 300−480 nm (extinction coefficients, ε, are seldom larger than 250 000 dm^3 mol^{-1} cm^{-1}) and the much weaker Q-band in the region of 600−700 nm (ε values are frequently less than 20 000 dm^3 mol^{-1} cm^{-1}).[21] Phthalocyanines also exhibit the Soret band ($320 \leq \lambda_{max} \leq 430$ nm; $\varepsilon \leq 80\,000$ dm^3 mol^{-1} cm^{-1}, that is, of much lower intensity than in porphyrins) and Q-bands ($630 \leq \lambda_{max} \leq 750$ nm; ε frequently approaching 250 000 dm^3 mol^{-1} cm^{-1}). Thus, the phthalocyanine Q-band is a stronger absorption than those of porphyrins.

A study of the regression of porphyrin properties to those of phthalocyanines are hampered in that phthalocyanines have four benzene rings annulated to the macrocyclic core, whereas porphyrins do not (Figure 1). Benzene annulated porphyrins, tetrabenzoporphyrins, are a class of porphyrins that is now attracting increasing attention,[22] but hybrid structures of benzoporphyrins and phthalocyanines bearing monoaza, diaza, and triaza apexes (meso atoms) are very much less studied. A recent review reports fewer than 150 papers have been published on these compounds.[23] However, of particular relevance to the present paper are those of Lever and Leznoff who described some electrochemical, spectroelectrochemical, and Langmuir−Blodgett film deposition studies[24] of peripherally substituted tetrabenzotriazaporphyrins, while Nyokong[25] reported on the electrochemical and photophysical properties of tin complexes of tetrabenzotriazaporphyrins. Kobayashi, Mack, and co-workers reported on the magnetic circular dichroism properties in relation to time-dependent density functional theory (TD-DFT) calculations of related copper complexes.[26]

Following the recent report describing an easy synthesis of metalated and metal-free octahexyl-substituted tetrabenzotriazaporphyrins (TBTAPs), tetrabenzodiazaporphyrins (TBDAPs), tetrabenzomonoazaporphyrins (TBMAPs), as well as tetrabenzoporphyrins (TBPs),[27] (compounds **1**−**4**, Scheme 1), we report herewith the first comparative electrochemical study of this unique series of compounds. Compounds **5a** and **5b**, referred to in the text as 2H-Pc and Cu-Pc, are the corresponding phthalocyanine derivatives where all four meso positions are occupied by nitrogen atoms, see Figure 1. Results from a spectroelectrochemical study of the oxidations and reductions of selected compounds are also presented. The effects obtained by systematically increasing the number of meso nitrogen atoms are related to their electronic spectra and quantified utilizing atomic electronegativities (Pauling scale). We also highlight the differences in binding energies of the different types of aza atoms in this series of compounds utilizing X-ray photoelectron spectroscopy.

2. EXPERIMENTAL SECTION

2.1. General. Solid reagents and solvents were from Aldrich or Merck and used as received unless otherwise stated. CH_2Cl_2 was dried by refluxing with CaH_2 under a nitrogen atmosphere and distilled directly before use. Tetrahydrofuran (THF) was dried over sodium wire. Compounds **1**−**4**,[27] **5a**,[13] **5b**,[8c] and $[N(^nBu)_4][B(C_6F_5)_4]$[28] were synthesized as described before.

2.2. Spectroscopy (UV−vis, ^{1}H NMR, XPS). UV−vis spectra were recorded using a Varian Cary 50 spectrophotometer and quartz cell of path length 1 cm utilizing THF as solvent.

^{1}H NMR spectra at 293 K were recorded on a Bruker Avance DPX 300 NMR spectrometer at 300 MHz with chemical shifts presented as δ values referenced to $SiMe_4$ at 0.00 ppm utilizing $CDCl_3$ or C_6D_6 as solvent.

X-ray photoelectron spectroscopy (XPS) data were recorded on a PHI 5000 Versaprobe system with monochromatic Al Kα X-ray source. Spectra were obtained using an aluminum anode (Al Kα = 1486.6 eV) operating at 50 μm, 12.5 W, and 15 kV energy (97 X-ray beam). Survey scans were recorded at constant pass energy of 187.85 eV and detailed scans of C, O, and N were recorded at constant pass energy of 29.35 eV, while the detail scans of Cu were recorded at pass energy of 58.7 eV with the analyzer resolution ≤0.5 eV. The background pressure was 2×10^{-8} mbar. The XPS data were analyzed utilizing Multipak version 8.2c computer software[29] using Gaussian−Lorentz fits (the Gaussian/Lorentz ratios were always >95%).

2.3. Electrochemistry. Cyclic voltammograms (CVs), square wave voltammograms (SWs), and linear sweep voltammograms (LSVs) were conducted using a Princeton Applied Research PARSTAT 2273 voltammograph running PowerSuite (Version 2.58) utilizing a standard three-electrode cell in a M Braun Lab Master SP glovebox filled with high-purity argon (H_2O and O_2 < 5 ppm). Experiments were performed at 20.0 ± 0.1 °C under argon on 1 mmol dm^{-3} solutions of **1**−**4** in dried distilled CH_2Cl_2 in the presence of 0.1 mol dm^{-3} $[N(^nBu)_4][B(C_6F_5)_4]$ as supporting electrolyte. A three-electrode cell was used consisting of a glassy carbon working electrode with surface area of 3.14 mm^2 pretreated by polishing on a Buehler microcloth first with 1 μm and then 1/4 μm diamond paste, a Pt-wire counter electrode, and an in-house constructed Ag/AgCl reference electrode constructed from a silver wire inserted into a solution of 0.1 mol dm^{-3} $[N(^{n}Bu)_4][B(C_6F_5)_4]$ in acetonitrile, in a luggin capillary with a vycor tip. Successive experiments under the same experimental conditions showed that all formal reduction and oxidation potentials were reproducible within 5 mV. All potentials in this study were experimentally referenced against the Ag/AgCl couple; decamethylferrocene (Fc*) was used as an internal standard. Decamethylferrocene has $E^{o\prime} = (E_{pa} - E_{pc})/2 = -610$ mV versus free ferrocene, $i_{pc}/i_{pa} = 0.98$, and $\Delta E_p = E_{pa} - E_{pc} = 66$ mV under our conditions. Data were exported to a spreadsheet program for manipulation to be reported referenced[30,31] against FcH/FcH^+ and diagram preparation as suggested by IUPAC.[30] Under our conditions $E^{o\prime}$ of ferrocene was found to be 412 mV versus our in-house constructed Ag/AgCl electrode. Caution must, however, be exercised in utilizing this $E^{o\prime}$ value as a universal constant. Changes in electrodes or cell construction from experiment to experiment caused this value to be between 362 and 426 mV.

2.3. Spectroelectrochemistry. Spectroelectrochemical measurements were conducted by placing an optically transparent thin-layer electrode (OTTLE) cell containing the redox-active components in the light beam of a Varian Cary 5000 near-IR spectrometer. The OTTLE cell was manufactured by the Amsterdam University according to Hartl's design[32] and consisted of a Pt mesh as working electrode, a platinum wire auxiliary electrode, and a silver wire reference electrode contained between two KBr windows 1 mm apart. The potential applied to the working electrode was controlled by a Princeton Applied Research PARSTAT 2273 electrochemical workstation interfaced with a personal computer and ramped between −0.2 and 2.0 V for oxidation studies and between 0 and −2.0 V versus a silver wire for reduction studies at a scan rate of either 0.125 or 0.250 mV s^{-1}. A UV–vis–NIR spectrum was recorded between 280 and 3000 nm at every 50 mV potential increase. The OTTLE cell was charged with DCM solutions of **1** and **4** (0.3 mmol dm^{-3}) in the presence of 0.1 mol dm^{-3} $[N(^{n}Bu)_4][B(C_6F_5)_4]$.

2.4. Density Functional Theory Calculations. DFT calculations of this study were performed with the hybrid functional uB3LYP[33,34] with the triple-ζ basis set 6-311G(d,p) on all atoms as implemented in the Gaussian 09 program package.[35] All complexes were optimized as doublets ($S = 1/2$).

3. RESULTS AND DISCUSSION

3.1. Materials. The compounds investigated in this study all carry eight hexyl chains at the so-called nonperipheral positions to serve as solubilizing groups. The synthesis of series **1**–**4**, Scheme 1, from a common precursor, namely, 3,6-dihexylphthalonitrile, using various equivalents of the Grignard reagent MeMgBr, has been reported in full elsewhere.[27] Initially obtained as the magnesium metalated derivatives, their formation is remarkable and indeed fortuitous insofar as comparable ranges of compounds have not been achieved under these conditions using precursors with substituents located at alternative positions.[23] There are in principle two isomeric tetrabenzodiazaporphyrins (TBDAPs) varying in the locations of the meso nitrogen atoms. Only the cis isomer, see Scheme 1, was recovered in sufficient quantities for full characterization and measurements. All magnesium metalated derivatives were readily demetalated to the metal-free analogues, denoted in the text as (2H−), and samples were then converted into the copper metalated derivatives (Cu−) with copper acetate.[27]

1,4,8,11,15,18,22,25-Octakis(hexyl)phthalocyaninato magnesium, denoted as Mg-Pc, was prepared as described before[27] by refluxing magnesium turnings, magnesium acetate, and 3,6-dihexylphthalonitrile in the presence of 1,8-diazabicycloundec-7-ene for 72 h in pentanol. Demetalation and copper insertion to obtain phthalocyanines **5a** (2H-Pc) and **5b** (Cu-Pc) was achieved in the same way as mentioned above for the preparation of the series **1a**–**4a** and **1b**–**4b**. All compounds are stable in air; they can be stored for extensive periods (years) at ambient temperatures under a normal open atmosphere in darkness.

3.2. UV–vis Spectroscopic Studies. The UV–vis spectra of macrocyclic compounds **1a**–**4a** and **1b**–**4b** bearing zero, one, two, or three nitrogen atoms in the available meso positions were recorded in THF and compared with those of normal porphyrins (i.e., those without benzene annulated to the pyrrole ring) and phthalocyanines **5a** and **5b**, which have four nitrogen atoms in the macrocyclic meso positions. Table 1 summarizes λ_{max} wavelengths and associated extinction coefficients ε of dominating peak maxima in the Q-band (visible) absorption region ($588 \leq \lambda_{max} \leq 733$ nm) and Soret band (UV) absorption region ($310 \leq \lambda_{max} \leq 441$ nm). The first observed difference relates to the spectra of normal porphyrins[21] compared to those of benzene-annulated tetrabenzoporphyrins **1a**, 2H-TBP, and **1b**, Cu-TBP. Soret band absorptions were approximately of equal intensity at similar wavelengths (424–441 nm, Table 1), but Q-band extinction coefficients increased more than threefold in magnitude from below 20 000 dm^3 mol^{-1} cm^{-1} for typical porphyrins[21] to 64 570 (2H-TBP, **1a**) or 109 650 dm^{-3} mol^{-1} cm^{-1} (Cu-TBP, **1b**, Table 1). This is the result of a larger conjugated π system and associated larger molecular moment.[26]

Table 1. Soret and Q-Band Absorption Maxima and Corresponding Extinction Coefficients of 1– 5 in THF

compound	Soret band λ_{max}, nm (ε)[a]	Q-band λ_{max}, nm (ε)[a]	$\Delta E^{o\prime}$, V[b]
1a: M = 2H, 0 × N_{meso} atoms	424 (204 170); 441 (275 420)	626 (64 570); 677 (52 480)	1.730
1b: M = Cu, 0 × N_{meso} atoms	430 (218 780)	639 (109 650); 661 (56 230)	1.611
2a: M = 2H, 1 × N_{meso} atoms	413 (114 820);433 (91 210)	588 (19 500); 639 (79 720); 682 (107 150)	1.685
2b: M = Cu, 1 × N_{meso} atoms	413 (104 710); 429, (112 200)	641 (66 070); 662 (117 490)	1.692
3a: M = 2H, 2 × N_{meso} atoms	393 (61 660)	600 (19 050); 656 (72 440); 690 (81 283)	1.683
3b: M = Cu, 2 × N_{meso} atoms	391 (81 283)	608 (14 820); 666 (165 960)	1.717
4a: M = 2H, 3 × N_{meso} atoms	361 (56 230); 401 (46 860)	644 (45 180); 675 (78 320); 716 (123 510)[d]	1.536
4b: M = Cu, 3 × N_{meso} atoms	361 (47 870); 395 (47 860)	676 (89 430); 700 (128 820)	1.657
5a: M = 2H, 4 × N_{meso} atoms	310 (39 810); 350 (51 290)	663 (39 810); 695 (97 720); 733 (117 490)[c]	1.540
5b: M = Cu, 4 × N_{meso} atoms	310 (38 020); 350 (50 120	635 (37 150); 665 (32 360); 700 (208 930)	1.695

[a] ε in units of dm^3 mol^{-1} cm^{-1}. [b] Data from section 3.4; $\Delta E^{o\prime} = E^{o\prime}_{wave\ 1} - E^{o\prime}_{wave\ 3}$, a measure of the HOMO–LUMO gap. [c] A relatively weak peak at 628 nm (ε = 23 990) is also observed. [d] A relatively weak peak at 615 nm (ε = 18 200) is also observed.

Figure 2, right lower, shows the UV–vis spectrum of Cu-TBP. Figure 2, left, exhibits the electronic spectrum of 2H-TBMAP, **2a**, as well as the adherence to the Beer–Lambert law of the Q-band of this complex. Like phthalocyanines, the metal-free tetrabenzoporphyrins **1a**–**4a** exhibited Q-band maxima that were split into Q_x and Q_y components together with some small intensity peaks adjacent to the major Q-band peaks. These additional lower intensity satellite peaks are the result of the lower symmetry that is imposed on **1a**–**4a** with the

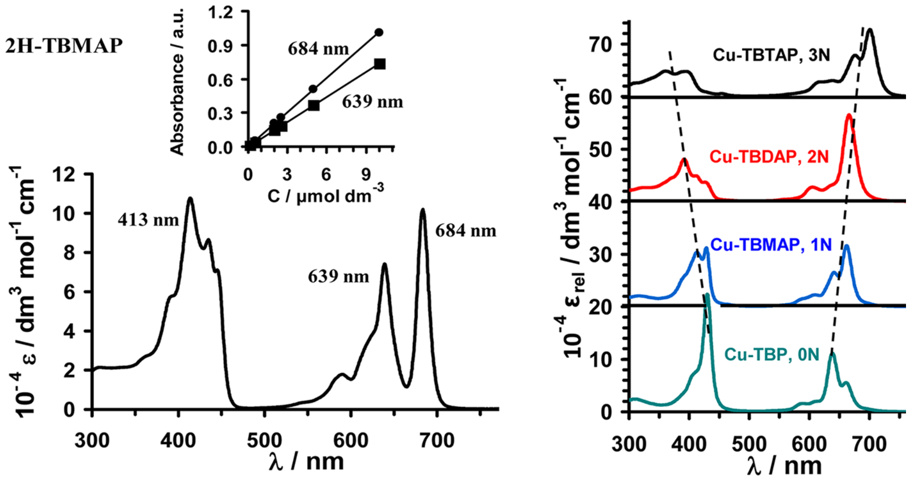

Figure 2. (left) UV−vis spectrum of 2H-TBMAP, **2a**, in THF showing extinction coefficients as a function of wavelength, and in the inset, the adherence of the Q_x and Q_y components of the Q-band at 684 and 639 nm, respectively, to the Beer−Lambert law, $A = \varepsilon cl$, up to $c = 10$ μmol dm^{-3} concentrations. (right) The Soret (UV) and Q (visible) bands of copper complexes **1b**−**4b** are shifted to shorter and longer wavelengths, respectively, as the number of nitrogen atoms in the meso position (denoted as 0N−3N) increases from zero to three.

introduction of additional N_{meso} atoms. For fully symmetrical metalated phthalocyanines, for example, **5** having 4 N_{meso} atoms, the Q-band manifests as a strong single peak due to D_{4h} symmetry. Of the Cu-TBP, Cu-TBMAP, Cu-TBDAP, and Cu-TBTAP derivatives, only Cu-TBDAP exhibited a single sharp Q-band with small satellite peaks.

The other metalated derivatives exhibited a Q-band split into at least two dominant Q-band components together with smaller adjacent peaks. This is again attributed to the lower complex symmetry arising from the introduction of more N_{meso} atoms.

Figure 2, right, shows the simultaneous red shift in peak maximum wavelengths of the Q-band and blue shift in peak maximum wavelengths of the Soret band in moving systematically from complex **1b** having no meso nitrogens through **2b** and **3b** to complex **4b** having three meso nitrogens. The Q-band λ_{max} of ca. 700 nm of nonperipherally substituted metalated phthalocyanines is one of the reasons why zinc phthalocyanines, in particular, are studied as second-generation photodynamic anticancer (PDT) drugs. Because light penetration through body tissue is the deepest for wavelengths between 620 and 850 nm,[36] PDT drugs that absorb strongly in these long-wavelength regions are most effective in destroying cancerous growths.

Here we explore if it is possible to relate Q-band λ_{max} differences to relative electron densities of the different macrocyclic cores. Figure 3, left, highlights the relationship between Q-band λ_{max} of compounds **1**−**4** and the sum of the group electronegativities, $\sum \chi_R$, of meso macrocyclic core atoms. $\sum \chi_R$ is a measure of the electron density of the macrocycle,[21] and R represents the meso atoms together with any substituent on them. Here, the meso atom groups R are either N or CH. By way of explanation, $\sum \chi_R$ for **3a** (or **3b**), which has two nitrogen meso atoms (Pauling electronegativity for nitrogen is $\chi = 3.04$) and two meso CH atom groups $\{\chi(\text{C}) = 2.55;\ \chi(\text{H}) = 2.20\}$, may be calculated as follows:

$$\begin{aligned}\sum \chi_R(3) &= 2\chi(\text{N}) + 2\{\chi(\text{C}) + \chi(\text{H})\}\\ &= 2(3.04) + 2(2.55 + 2.20)\\ &= 15.58\end{aligned}$$

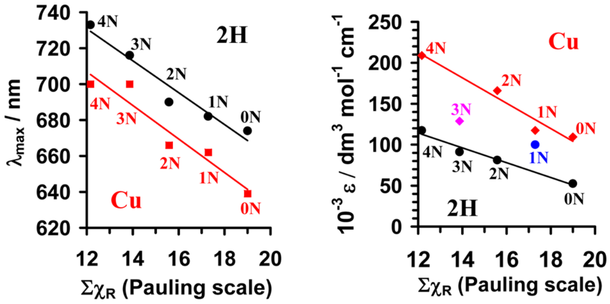

Figure 3. (left) Relationship between the most intense Q-band wavelength and $\sum \chi_R$ for metal-free (black line, top) and copper complexes (red line, bottom) **1**− **5**. The notation 0N through 4N denotes the number of meso nitrogen atoms in each case. (right) Relationship between extinction coefficient ε and $\sum \chi_R$ for metal-free (black line, bottom) and copper complexes (red line, top). The mauve point for the Cu line (3N) and the blue point for the metal-free line (1N) do not fit the trend set by the other complexes.

Macrocycles with smaller $\sum \chi_R$ values (e.g., 13.87 Pauling units for **4**) are less electron-withdrawing than macrocycles with larger $\sum \chi_R$ values (e.g., 19.00 Pauling units for **1**). From Figure 3 it follows that an easy way to predict or compare the shifts of the Q-band peak maxima is simply to calculate $\sum \chi_R$ and relate the two quantities to each other on a suitable calibration curve. We have in previous work also shown that this approach is feasible for non-hydrogen meso substituents, for example, ferrocenyl and C_6F_5 in relating electrochemical properties of meso-substituted porphyrins to $\sum \chi_R$.[21]

A further observation from Figure 3, right, and Table 1 relates to extinction coefficients. For TBP complexes having no meso nitrogen atoms, the Q-band maximum was much smaller than the Soret band maximum, while for TBMAP complexes having one meso nitrogen atom, extinction coefficients of the most intense Soret and Q-band peaks were in the same region (between 107 150 and 117 490 dm^3 mol^{-1} cm^{-1}, Table 1). For TBDAP, TBTAP, and phthalocyanine complexes, the Soret band becomes less intense compared to the Q-band as the number of meso nitrogen atoms increases from two to four. Figure 3, right, highlights how the Q-band ε values of **1b**−**5b** decrease from 208 930 for **5b** to 56 230 dm^3 mol^{-1} cm^{-1} for **1b**

Table 2. Binding Energies and Ratios of the Different Nitrogen and Copper Peaks Obtained from Gaussian Fitting of Detailed XPS Scans

	N_{inner} or N_{Cu} 1s, eV (atomic %)	$(\underline{N}H)_{inner}$ 1s, eV (atomic %)	N_{meso} 1s, eV (atomic %)	Cu $2p_{3/2}$, eV	Cu $2p_{3/2}$ shake -up, eV
2H-TBP, **1a**	397.8 (50%)	399.7 (50%)			
Cu-TBP, **1b**	398.4 (100%)			934.7	943.0
2H-TBMAP, **2a**	397.8 (40%)	399.7 (40%)	398.4 (20%)		
Cu-TBMAP, **2b**	398.2 (80%)		399.0 (20%)	934.6	942.8
2H-TBDAP, **3a**	397.8 (33.3%)	399.5 (33.3%)	398.5 (33.3%)		
Cu-TBDAP, **3b**	398.3 (66.7%)		398.0 (33.3%)	934.8	943.5
2H-TBTAP, **4a**	397.7 (28.6%)	400.1 (28.6%)	398.6 (42.9%)		
Cu-TBTAP, **4b**	398.0 (57.1%)		398.4 (42.9%)	934.8	943.0

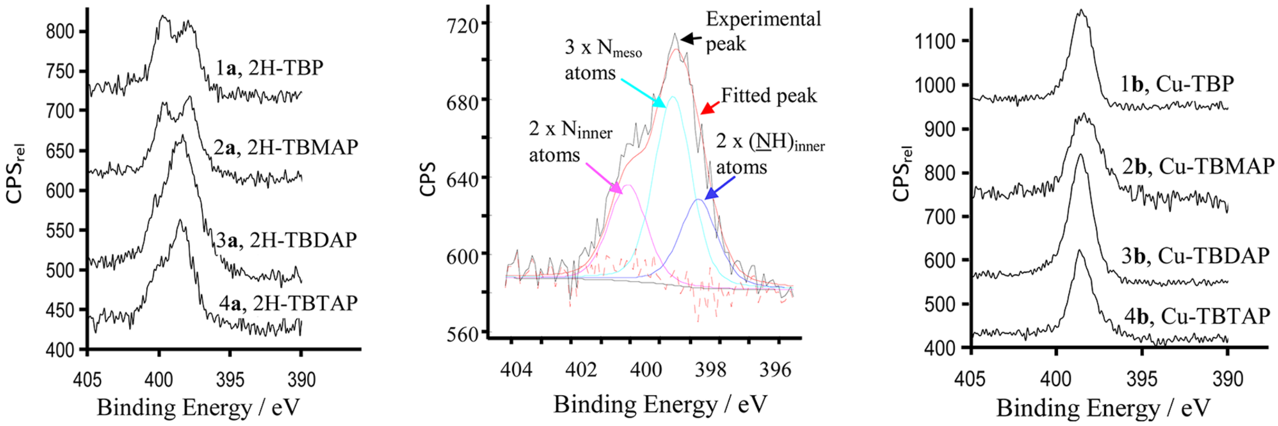

Figure 4. (left) Detailed scans of N 1s XPS spectra of the nitrogen region of metal-free macrocycles **1a**−**4a**. (middle) The N 1s XPS spectrum of **4a**, showing three Gaussian peaks fitted in a ratio of 2:3:2, regenerates the experimentally measured spectrum well. (right) Detailed N 1s XPS spectra of the nitrogen region of copper-containing macrocycles **1b**− **4b**. CPS = counts per second, rel = relative.

as the macrocyclic core density expressed as $\sum\chi_R$ changes upon decreasing the number of meso nitrogen from four to zero. While ε values are frequently related to transition moments, fundamentally, any (molecular) moment is related to dipoles in the molecular structure. Dipoles are a direct consequence of regions of a molecule being more electron-rich than others. The latter depends on the electronegativity of atoms in the more electron-rich region compared to the electronegativity of atoms in the less electron-rich molecular region. The relationship observed in Figure 3, right, is therefore not surprising. The Q-band peak maximum wavelengths (eqs 1 and 3) and extinction coefficients (eqs 2 and 4) of related compounds may be estimated from eqs 1−4 that were obtained by fitting the data of Figure 3.

Metal-Free Complexes.

$$\lambda_{max} = -8.8889 \sum \chi_R + 837.49;\ R^2 = 0.95 \tag{1}$$

$$\varepsilon = -9.0632 \sum \chi_R + 222.94;\ R^2 = 0.97 \tag{2}$$

Copper (or Metalated) Complexes.

$$\lambda_{max} = -9.3567 \sum \chi_R + 819.2;\ R^2 = 0.92 \tag{3}$$

$$\varepsilon = -15.477 \sum \chi_R + 398.26;\ R^2 = 0.96 \tag{4}$$

3.3. X-ray Photoelectron Spectroscopy. The metal-free complex **1a** has two types of nitrogen in its macrocyclic core, while **2a**−**4a** have three types in their cores. These are two N_{inner}, two $(\underline{N}H)_{inner}$ atoms, and zero, one, two, three, or four meso nitrogen atoms, N_{meso}. In copper complexes **1b**−**4b** the two N_{inner} and two $(\underline{N}H)_{inner}$ atoms collapse into four identical N_{Cu} atoms (see Scheme 1 to identify the different types of N atoms). An attempt was made to distinguish between these different types of nitrogen atoms utilizing X-ray photoelectron spectroscopy (XPS) by determining their binding energies. The binding energy of the copper atom in these complexes was also determined. Table 2 summarizes the binding energies and ratios of these atoms within the ring structures of types **1**−**4**.

In the detailed scans of nitrogen 1s XPS spectra of the metal-free compounds 2H-TBP, **1a**, and 2H-TBMAP, **2a** (Figure 4), two well-resolved peaks can be observed that are assigned to the inequivalent inner ring nitrogen atoms, N_{inner} at 397.8 eV and the $(\underline{N}H)_{inner}$ atoms at 399.7 eV. This assignment is in agreement with previously reported XPS assignments of these nitrogen atom types in both phthalocyanines and porphyrins.[37] A clear assignment of the N_{meso} atom in **2a** was not directly possible, but to identify the binding energy of N_{meso} atoms, the XPS spectrum of **4a** was helpful. Compound **4a**, 2H-TBTAP, has three N_{meso} atoms, and this allowed the N_{meso} peak to rise strongly above and in between the peaks of the N_{inner} (397.7 eV) and the $(\underline{N}H)_{inner}$ (400.1 eV) atoms at a binding energy of 398.6 eV, Figure 4, left. Fitting of the experimental N 1s XPS spectrum of macrocycle **4a** to theoretical peaks for these three different types of nitrogen atoms confirmed the nitrogen atoms are present in this macrocycle in a ratio of $N_{inner}/N_{meso}/(\underline{N}H)_{inner}$ = 2:3:2, Figure 4, middle. Upon assigning the binding energy of N_{meso} atoms of **2a** and **3a** as indicated in Table 2, the atom ratio of $N_{inner}/N_{meso}/(\underline{N}H)_{inner}$ could also be verified for these two complexes as 2:1:2 and 2:2:2, respectively.

Figure 4, right, shows the comparative detailed N 1s XPS spectra of the copper-containing macrocycles **1b**−**4b**. Clearly, when a metal (in this case copper) is complexed to the macrocycle, resolution of the different types of nitrogen 1s peaks disappears. For **1b**, merging of the N_{inner} and $(\underline{\mathrm{NH}})_{\mathrm{inner}}$ peaks of the metal-free derivatives into one peak assignable to four identical N_{Cu} atoms was expected, but the observation that N_{meso} atoms experience a similar chemical environment in complexes **2b**−**4b** was surprising. Complex **1b** (Cu-TBP, no N_{meso} atoms) only shows one well-defined nitrogen 1s peak, and only one Gaussian peak is fitted into this peak at a binding energy of 398.4 eV. The best fit to all five nitrogen atoms of Cu-TBMAP, **2b**, was achieved by assigning a binding energy of 398.2 eV to the N_{meso} atom and 399.0 to the four N_{Cu} atoms, Table 2. Although these two binding energies for the two types of nitrogens in **2b** differ significantly, we could not meaningfully fit similar peaks to the experimentally obtained spectra of the other copper complexes, see Figure 4 right. The best fit to the experimental data of **3b** was achieved when the binding energy of the 4 × N_{Cu} and 2 × N_{meso} atoms was only 0.3 eV apart, while for **4b** the best fit was achieved when the binding energy of the 4 × N_{Cu} and 3 × N_{meso} atoms was only 0.4 eV apart, Table 2. These differences are too little to be considered significant.

Cu $2p_{3/2}$ peaks in the XPS spectra of the copper region of **1b**−**4b** all appeared at a binding energy of ca. 934.7 eV, while the Cu $2p_{1/2}$ peaks were detected at ca. 954.6 eV. The lack of different Cu binding energies in **1b**−**4b** showed that the extra N_{meso} atoms in the outer ring of the macrocycles have a negligible influence on the chemical environment of the copper, Table 2. Similar to previously reported copper-containing phthalocyanines,[38] the spectra also showed clear copper $2p_{3/2}$ and $2p_{1/2}$ shakeup peaks at ca. 943.0 and 962.9 eV, respectively; these are associated with about 9 eV higher binding energies than those of the main peaks, Figure 5.

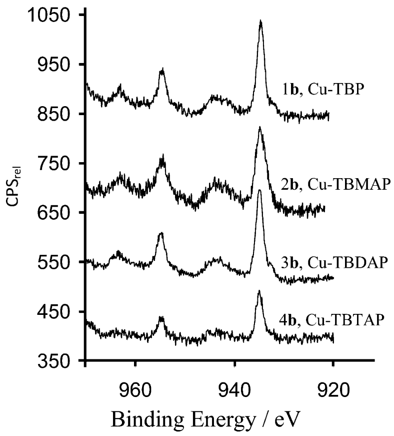

Figure 5. Detailed copper $2p_{3/2}$ XPS spectra of the copper region of macrocycles **1b**−**4b** showing the Cu $2p_{3/2}$ binding energy at ca. 934.7 eV as well as copper shakeup energies at ca. 943.0 eV. The Cu $2p_{1/2}$ and Cu $2p_{1/2}$ shakeup signals are at 954.6 and 962.9 eV, respectively. CPS_{rel} = relative counts per second.

3.4. Density Functional Theory Calculations.

The first two oxidation processes of any complex in general would involve the successive removal of electrons from the highest occupied molecular orbital (HOMO) and HOMO−1 of the complex, while adding electrons to the lowest unoccupied molecular orbital (LUMO) leads to reduction. Since the electrochemical oxidations and reductions of copper(II) phthalocyanines occur on the phthalocyanine ring and not on the central Cu(II),[39] while the first reduction of certain copper(II) porphyrins[40] and corroles[41] occur on the metal, a quantum chemical study by means of DFT calculations was performed to establish the character of the frontier orbitals of the copper complexes **1b**−**5b**. To aid understanding of the electrochemical redox processes, the calculations were extended to structures where the R substituents (see Figure 1 and Scheme 1 for the position of R) were varied between R = H, CH_3, C_2H_5, *n*-C_3H_7, and *n*-C_6H_{13}. Supporting Information, Figure S1 shows the four frontier orbitals of the unsubstituted (R = H) equivalents of complexes **1b**− **5b**. For all five of these R = H complexes the HOMO and HOMO−1 are of $a_{2u}(\pi)$ ligand character, implying that the first two oxidation processes, labeled 1 and 2 in Figure 8 (Electrochemistry Section), should be ring-based. Generally good relationships are obtained between the DFT-calculated HOMO energy (E_{HOMO}) and the formal reduction potential $E^{o\prime}$ of a series of related complexes of which the redox processes are of the same origin (e.g., all ligand or all metal-based).[42] The mathematical relationship between $E^{o\prime}$ and E_{HOMO} for these R = H complexes equivalent to **1b**−**5b** [see graph shown in Supporting Information, Figure S2a] is

$$E^{o\prime} = -0.65E_{\mathrm{HOMO}}(\mathrm{eV}) - 3.22;\ R^2 = 0.99 \qquad (5)$$

$E^{o\prime}$ represents the first oxidation of these complexes in V versus $\mathrm{FcH/FcH^+}$; values used for $E^{o\prime}$ in this relationship are from Section 3.5 below; see also Table 3.

No similar relationship is found between the first reduction potential and the DFT-calculated LUMO energy (E_{LUMO}) of complexes equivalent to **1b**−**4b** but having R = H. In particular, the complex equivalent to **1b** does not fit the trend (Figure S2b). From the visualization of the LUMOs (Figure S1) it is observed that the LUMO and LUMO+1 of the unsubstituted (R = H in Figure 1) equivalents of complexes **3b**−**5b** are ligand-based; they have typical $e_g(\pi^*)$ character. The first two reduction processes of **3b** and **4b** (labeled 3 in the electrochemistry section below, Figure 8) are thus expected to be both ligand-based. Experimentally it was found in the electrochemistry section below that the difference in the first and second reduction potentials of **3b** and **4b** is ca. 0.420 V (see potentials summarized in Table 3). However, the R = H equivalents of **1b** and **2b** have 65% Cu-d character for their LUMOs (Figure S1) implying that for these two complexes the first reduction process (the equivalent of wave 3 in Figure 8) is a Cu(II) reduction and not a ring-based process. A recalculation for **1b** with R = CH_3 still showed Cu(II) reduction to be the first reduction process, but for **2b** and its homologues (R = CH_3, C_2H_5, *n*-C_3H_7, *n*-C_6H_{13}) the LUMO energy levels were such that the first reductive process could be assigned to a ring-based reduction process. To confirm the Cu(II) and the macrocycle as the redox centers for **1b** and **2b** with R = *n*-C_6H_{13}, the DFT-optimized LUMOs of these complexes were calculated, and they are presented in Figure 6. While the LUMO of **1b** has 65% Cu-d character, the LUMO of **2b** is ligand-based. The LUMO+2 of **2b** is of Cu-d (64%) character. This result is consistent with the first reduction of **1b** to involve the Cu(II) center, while the first reduction processes of **2b** does not involve Cu(II) but is ligand (macrocycle)-based.

An interesting observation concerning the DFT-optimized geometry of **1b** and **2b** necessitates further consideration. The macrocycle of **1b** is flat with a saddling angle ϕ of 3.8°, while **2b** is considerably more saddled with ϕ = 15.4°; see Figure 7.

In comparing tetrabenzomonoazaporphyrin complexes with alkyl chains R of increasing size, an increase in saddling angle as

Table 3. Cyclic Voltammetry Data (potentials vs FcH/FcH$^+$) of ca. 0.5 mmol dm^{-3} Solutions of Decamethylferrocene and 1−4 in CH_2Cl_2 Containing 0.1 M $[N(^nBu)_4][B(C_6H_5)_4]$ at 25 °C and Scan Rate of 100 mV s^{-1}

wave	E_{pa}, V	ΔE_π, μς	$E^{o\prime}$, V^a	i_{pa}, μA	i_{pc}/i_{pa}	wave	E_{pa}, V	ΔE_π, μς	$E^{o\prime}$, V^a	i_{pc}, μA	i_{pc}/i_{pa}
		ferrocene						decamethylferrocene			
	−0.035	70	0.000	2.08	0.96	**Fc***	−0.043	66	−0.610	2.05	0.98
		2H-TBP, 1a, 0 N_{meso}						**Cu-TBP, 1b, 0 N_{meso}**			
4	−2.052	148	−2.126	2.30	0.95^b	**4**	*c*	*c*	*c*	*c*	*c*
3a	−1.734	98	−1.783	*d*	*d*	**3**	−1.664	140	−1.734	2.10	0.91^b
3b	−1.642	68	−1.676	2.10^d	0.95^{b,d}						
1a	0.000	112	−0.056	*d*	*d*	**1a**	−0.081	84	−0.123	*d*	*d*
1b	0.112	114	0.055	2.10^d	0.78^d	**1b**	−0.001	80	−0.041	1.78	0.82
2a	0.683	80	0.643	*d*	*d*	**2a**	0.651	90	0.606	*d*	*d*
2b	0.757	70	0.722	2.30^d	0.98	**2b**	0.733	80	0.693	1.78	1.08
		2H-TBMAP, 2a, 1 N_{meso}						**Cu-TBMAP, 2b, 1 N_{meso}**			
4	−2.020	106	−2.073	1.67	0.94^b	**4**	*c*	*c*	*c*	*c*	*c*
3	−1.644	106	−1.697	1.67	0.98^b	**3**	−1.721	114	−1.778	2.20	0.97^b
1	0.028	80	−0.012	1.57	0.95	**1**	−0.029	114	−0.086	2.22	0.94
2	0.764	106	0.711	1.68	0.98	**2**	0.647	108	0.701	2.39	0.956
		2H-TBDAP, 3a, 2 N_{meso}						**Cu-TBDAP, 3b, 2 N_{meso}**			
4	−1.920	80	−1.960	1.42	0.99^b	**4**	−2.148	116	−2.206	2.20	0.89^b
3	−1.586	92	−1.632	1.4	0.99^b	**3**	−1.724	98	−1.773	2.10	0.91^b
1	0.106	110	0.051	1.42	0.90	**1**	0.011	134	−0.056	2.21	0.87
2	0.770	96	0.722	1.40	0.97	**2**	0.758	98	0.709	2.31	0.93
		2H-TBTAP, 4a, 3 N_{meso}						**Cu-TBTAP, 4b, 3 N_{meso}**			
4	−1.826	80	−1.866	2.12	0.96^b	**4**	−2.022	96	−2.070	2.91	0.95^b
3	−1.420	80	−1.460	2.14	0.97^b	**3**	−1.604	104	−1.656	2.88	0.96^b
1	0.126	100	0.076	2.14	0.91	**1**	0.070	138	−0.001	2.80	0.98
2	0.758	98	0.709	2.14	0.98	**2**	0.828	106	0.775	2.99	0.97

$^a\Delta E^{o\prime} = E^{o\prime}_{\text{wave 1}} - E^{o\prime}_{\text{wave 3}}$, a measure of the HOMO−LUMO gaps and related to λ_{max} of the Q-band, is summarized in Table 1. $^b i_{pa}/i_{pc}$. Current ratios were always taken to be (reverse scan current)/(forward scan current). ^{c}Peaks were not detected in this solvent. ^{d}Because of closeness of neighboring peak (possible dimerization), values are estimates only utilizing the main peak. Because of poor peak resolution, currents for the minor peak were not measured, but see LSV traces in Supporting Information for relative sizes.

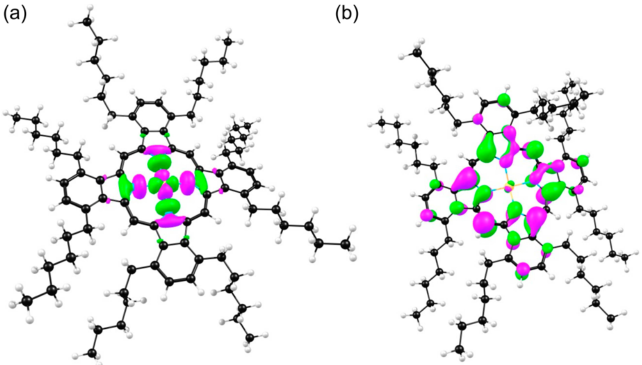

Figure 6. Presentation of the LUMO of DFT-optimized (a) **1b** and (b) **2b**. The MO plots use a contour of 30 e/nm^3. Color code of atoms: Cu (orange), C (black), N (blue), H (white).

a result of increased steric crowding was calculated. Saddling angles were for R = H (ϕ = 0°), R = CH_3 (ϕ = 13.1°), C_2H_5 (ϕ = 14.9°), n-C_3H_7 (ϕ = 16.2°), and n-C_6H_{13} (ϕ = 15.4°). The result of the increase in saddling angle is that the Cu-based LUMO of tetrabenzomonoazaporphyrin with R = H becomes destabilized with increased alkyl chain size; it becomes LUMO +1 when R = CH_3 and LUMO+2 for larger alkyl chains (R = C_2H_5, n-C_3H_7, and n-C_6H_{13}). This implies that Cu(II) reduction represents the first reductive process for **2b** when R = H, but it becomes the second reductive process of **2b** if R = CH_3 and the third reductive process for **2b** with alkyl chains R = C_2H_5, n-C_3H_7, and n-C_6H_{13}. This striking result may be visualized with the energy level diagram shown in Supporting Information, Figure S3 and the molecular orbital plots shown in Supporting Information, Figure S4.

3.5. Electrochemistry.

The influence of the different number of N_{meso} atoms on the redox properties of the macrocylic derivatives **1a**−**4a** and **1b**−**4b** was investigated by cyclic voltammetry (CV), square wave voltammetry (SW), and linear sweep voltammetry (LSV) in CH_2Cl_2 utilizing 0.1 mol dm^{-3} $[N(^nBu)_4][B(C_6H_5)_4]$ as supporting electrolyte. Use of this electrolyte minimizes ion pair formation between charged redox-generated substrate intermediates and supporting electrolyte ions.[43] CVs are shown in Figures 8 and 9, as well as Supporting Information, Figure S5; Table 3 summarizes data. In general, within the potential limits that the solvent (CH_2Cl_2) allow, four quasi-reversible ring-based redox processes were observed. Potential scanning generally commenced at −800 mV versus FcH/FcH$^+$ in the positive direction, and peaks were labeled in the order they were observed as follows: Fc* is the label of the internal standard, decamethylferrocene. Peaks 1 and 2 identify the first and second ring-based oxidative (anodic) processes, while peaks 3 and 4 identify the first and second reductive (cathodic) ring-based redox processes, except for 1b, see discussion below.

Figure 8 highlights how the increase in number of meso nitrogens systematically increases the formal cathodic wave potentials, waves 3 and 4, of compound types **1**−**4**. The total increase to larger potentials from **1a** to **4a** (values for the copper derivatives **1b** to **4b** are in brackets) for wave 4 was 260 mV (136, only Cu compounds **3b** and **4b** exhibited this wave),

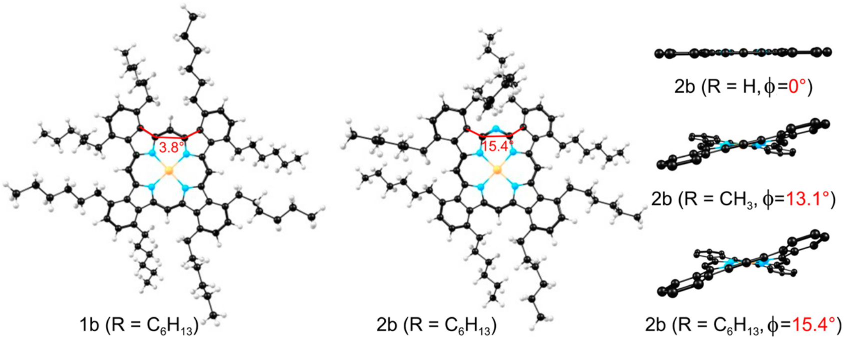

Figure 7. Geometry of tetrabenzoporphyrin **1b** (R = *n*-C$_6$H$_{13}$, left) and differently substituted tetrabenzomonoazaporphyrin derivatives (middle and right) showing the degree of saddling. H atoms and R groups were removed from figures on the right for clarity. Color code of atoms: Cu (orange), C (black), N (blue), H (white).

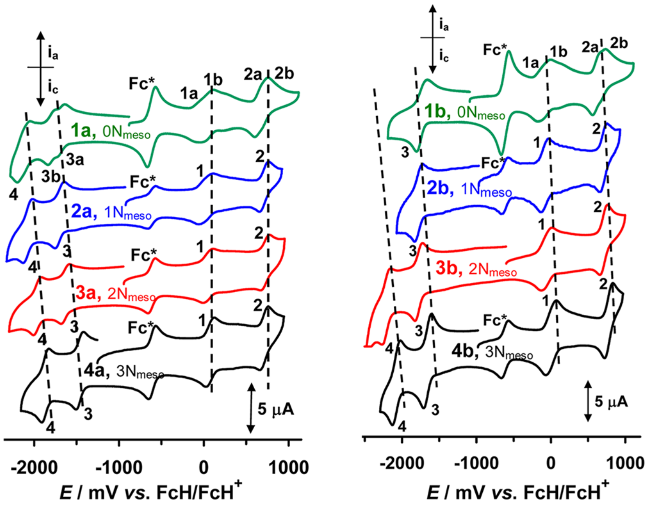

Figure 8. CVs of ca. 0.5 mmol dm^{-3} solutions of 2H-TBP (**1a**, green), 2H-TBMAP (**2a**, blue), 2H-TBDAP (**3a**, red), and 2H-TBTAP (**4a**, black) on the left and, on the right, CVs of Cu-TBP (**1b**, green), Cu-TBMAP (**2b**, blue), Cu-TBDAP (**3b**, red), and Cu-TBTAP (**4b**, black) at 100 mV s^{-1} in CH$_2$Cl$_2$/0.1 mol dm^{-3} [N(^{n}Bu)$_4$][B(C$_6$H$_5$)$_4$]. The notation 0N to 4N denotes the number of meso nitrogen atoms in each compound.

while for wave 3 it was 323 (78) mV. For the anodic waves 1 and 2, these drifts were 132 (122) and 66 (169) mV, respectively; see Table 3. From the DFT results described in the previous section, all these observed redox reactions are assigned to a ring-based process except wave 3 for **1b**, which represents a Cu(II) reduction. At a scan rate of 100 mV s^{-1}, peak potential differences were in the region of $80 \leq \Delta E_p < 148$ implying more quasi electrochemical reversibility than true electrochemical reversibility, this despite the internal marker Fc* showing ΔE_p = 66 mV in the same solution as the analyte. Electrochemical reversibility is characterized by ΔE_p values of 59 mV.[44] Peak current ratios were much closer to ideal with only wave 1b of 2H-TBP, **1a**, deviating significantly from unity; see Table 3.

TBP complexes **1a** and **1b** showed signs of dimerization at the redox processes associated with waves 1, 2, and 3 for **1a** and waves 1 and 2 for **1b** because these processes separate into two components "a" and "b", Figure 8, upper. SW experiments show this peak splitting much more clearly (Supporting Information, Figure S5). The LSV at 2 mV s^{-1} shows the current of all "a" and "b" components of waves 1, 2, and 3 for compound **1a** and waves 1 and 2 for **1b** are equal in size (Supporting Information, Figure S5). A similar wave pattern that was proved to be associated with dimerization was also observed in the Cd phthalocyanine complexes we reported earlier.[15,31e]

We conclude that at the concentrations used for CV studies, namely, 0.5 mmol dm^{-3}, both **1a** and **1b** exist as associated dimers in the ground, first oxidized and second oxidized states. 2H-TBP, **1a**, also exists as an associated dimer until the first reduced state is reached, but then the two positive charges, one on each half of the associated dimer, probably induces dimer dissociation due to electrostatic repulsive forces. Dissociation is complete before the second reductive redox step is initiated because wave 4 shows no sign of peak splitting into two components. For the copper derivative **1b**, wave 1 (the first oxidative step) is clearly representative of two equal-sized redox steps, while wave 3 (the first reductive step) shows no sign of two peak components; see Figure 8 and Supporting Information, Figure S5. This is consistent with an equilibrium existing between Cu-TBP monomers and dimers in the neutral ground state with the dimer more easily oxidized than reduced and the monomer more easily reduced than oxidized. These results imply the metal-free dimer is more strongly associated than the copper dimer. Scheme 2 provides an electrochemical mechanism explaining the redox observations of **1a** by incorporating knowledge that could be gathered from DFT calculations, electrochemical measurements and spectroelectrochemical measurements (see next section).

Figure 9 simultaneously shows the influence of scan rate and copper insertion utilizing the TBTAP derivatives, **4**, as an example. Formal redox potentials are scan rate independent. Copper insertion leads to a substantial lowering in the redox potential of waves 4 (204 mV), 3 (196 mV), and 1 (77 mV), but wave 2, representative of the second oxidative redox process, was shifted 66 mV to a larger potential. Complexes **1**–**3** showed the same trend for all observed waves 1–4; see Table 1 and Figure 10.

Figure 10 relates redox potentials of waves 1–4 with the sum of the group electronegativity of all meso N and CH atom groups, $\sum \chi_R$. As was the case with the electronic spectra peak maximum wavelengths and extinction coefficients, a definite relationship between $E^{o\prime}$ and $\sum \chi_R$ exists and implies that, as the macrocycle core becomes more electron-withdrawing (i.e., larger $\sum \chi_R$ values) with decreasing number of meso nitrogen atoms, redox potentials decrease.

The HOMO is the orbital from which an electron is removed in the first oxidation process, in Figures 8 and 10, this process is denoted as wave 1. During the first reduction process an

Scheme 2. Mechanism Explaining the Redox Electrochemistry of 2H-TBP 1a[a]

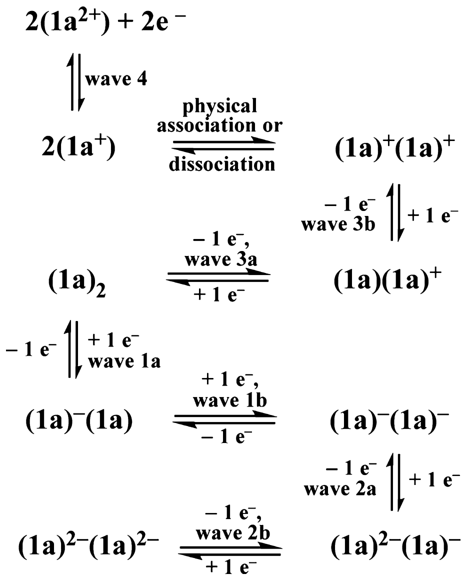

[a] Each step represents a one-electron transfer per molecular fragment. For **1b**, the most notable difference would be wave 3, which involves a Cu(II) reduction, while wave 4 would be absent.

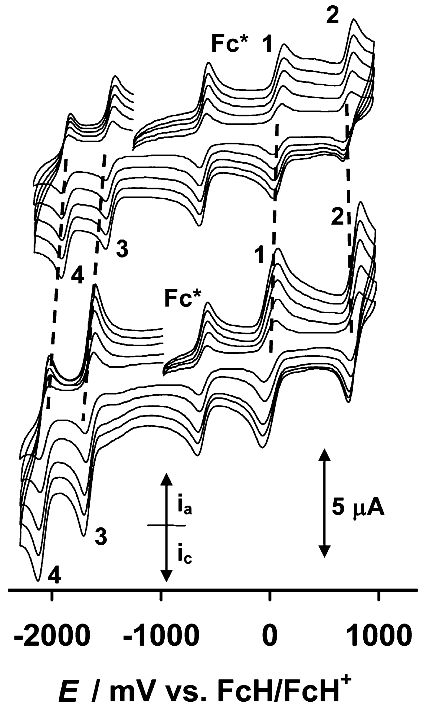

Figure 9. CVs of ca. 0.5 mmol dm^{-3} solutions of 2H-TBTAP (**4a**, upper) and Cu-TBTAP (**4b**, lower) in CH_2Cl_2/0.1 mol dm^{-3} $[N(^nBu)_4][B(C_6H_5)_4]$ at scan rates 100, 200, 300, 400, and 500 mV s^{-1}.

electron is inserted in the LUMO (wave 3). Waves 1 and 3 (as well as 2) for the copper-free complexes **1a**–**4a** and waves 1 and 2 for the copper complexes **1b**–**4b** exhibit a linear relationship, which is consistent with each of the electron-transfer processes originating from the same redox site, namely, a ring-based process according to the DFT calculations described in Section 3.4. However, for wave 3 of the copper complexes, no linear relationship was observed. This is consistent with the DFT result that suggests, for **1b** ($N = 0$), wave 3 represents a Cu(II) reduction and not a ring-based macrocyclic reduction. Wave 4 was only observed for **3b** and **4b**, and the DFT calculations showed it to represent a ring-based redox process. The slope of the connecting line of these two wave 4 points is also negative as for the other straight lines. The difference in energy between the HOMO and LUMO orbitals is the energy that is generally associated with excitation to generate the spectroscopic Q-band. Table 1 summarizes calculated $\Delta E^{o\prime} = E^{o\prime}_{\text{wave 1}} - E^{o\prime}_{\text{wave 3}}$ values. No clear relationship between the most intense absorption Q-band wavelength and $\Delta E^{o\prime}$ exists (Figure S6, Supporting Information), implying a single orbital explanation of $\lambda_{\max}$ values is an oversimplification. In the case of compounds of type **1**–**4**, this was further amplified in that in some cases wave 3 is a ring-based redox processes and in other cases it is copper based.

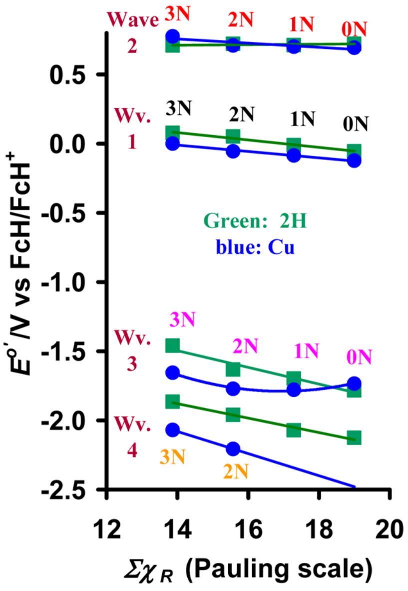

Figure 10. Relationship between $E^{o\prime}$ of redox waves 1–4 and $\sum\chi_R$ for metal-free (green line) and copper complexes (blue line) **1**–**4**. The notation 0N to 4N denotes the number of meso nitrogen atoms in each compound.

3.6. Spectroelectrochemistry.

The spectroelectrochemical properties of compounds of type **1** and **4** were investigated as representative examples of the present compound series. Figure 11 shows the spectral changes of **1a**, 2H-TBP, during reductive electrochemistry, that of **4b**, Cu-TBTAP, during oxidative redox chemistry, and those of **4a**, 2H-TBTAP, during reductive as well as oxidative redox processes. Table 4 provides spectroscopic data of the spectral changes as a result of changes in electrochemical oxidation states. Figure S7, Supporting Information, provides selected spectra of all available spectroelectrochemical results of **1** and **4**. Studies were performed utilizing an OTTLE cell of Hartl's[32] design.

Complex **1b** exhibited only one cathodic (reductive) redox process in the solvent potential window, while two consecutive reductive redox processes were observed for **1a**, **4a**, and **4b** during the electrochemical study of compounds of type **1** and **4** (Figure 8, Table 3). Upon following these redox processes spectroscopically, the Q-band intensity was substantially lowered in all cases except for **1b** in the first reductive redox process (Figure 11, Table 4, and Supporting Information, Figure S7). This would normally be consistent with ring-based

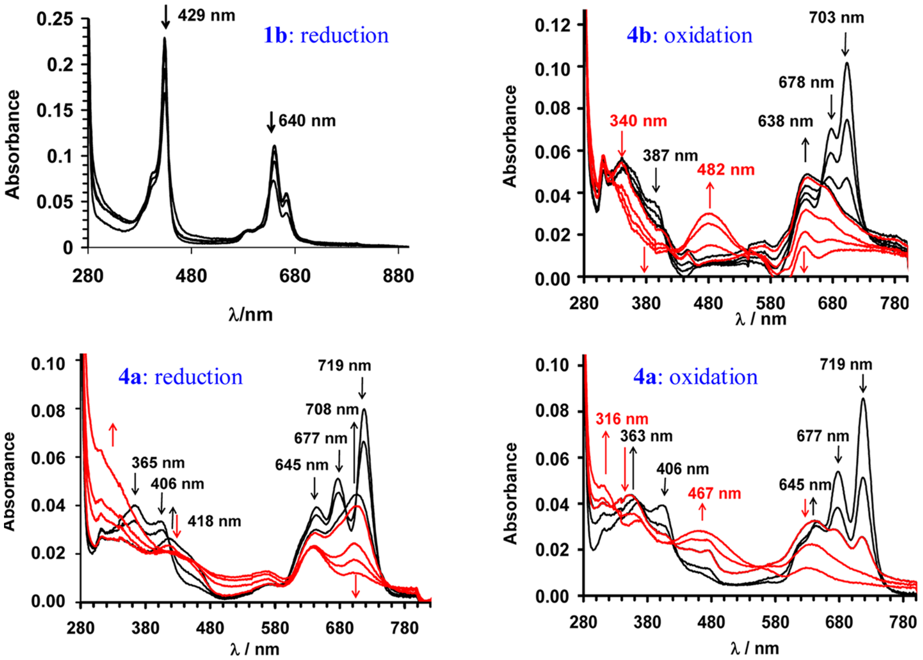

Figure 11. UV−vis spectra generated during reduction (left column figures) of Cu-TBP (**1b**, upper left) and 2H-TBTAP (**4a**, lower left), or during oxidation (right column figures) of Cu-TBTAP (**4b**, upper right) and 2H-TBTAP (**4a**, lower right). The first oxidative or reductive redox process is highlighted by black spectra, and the second with red spectra. The color-coded arrows show the direction in which peaks either increased or decreased in intensity; wavelengths on top of each arrow correspond to peak maximum wavelengths.

reductions for the copper complex and not reduction of the Cu(II) ion[45] (because no clear shift in maximum absorption wavelength was observed). However, in the case of **1b**, the lowering of the Q-band is too weak to be accounted for by a ring-based reduction. The alternative assignment for **1b** would be a Cu(II) reduction. Although one can see a lowering of the Q-band λ_{max} from 640 to 632 nm, the lowering is very subtle and not clearly indicative of Cu(II) reduction. This uncertainty was removed by the DFT calculation results that clearly indicated the first reductive redox process for **1b** to be copper-based and not ring-centered.

At the end of the first reduction, Q-band *x* and *y* components (for **1a**) and *x*, *y*, and *z* components (for **4a**) amalgamated into one low-intensity prominent peak at 633 nm for **1a** and low-intensity Q_x and Q_y components at 707 and 645 nm, respectively, for **4a**. Spectroscopic changes at the Soret band were more pronounced during the second redox process, especially for the metal-free complexes **1a** and **4a** (Figure 11 and Supporting Information, Figure S7).

With respect to the anodic (oxidative) redox processes, **1a**, **1b**, **4a**, and **4b** all exhibit two consecutive steps; see Figure 8 and Table 3. Spectroscopically, a general feature that accompanied the first electrochemical oxidation was disappearance of the Q_x component, that is, the longest wavelength Q-band absorption at 639−728 nm for all four complexes. At the end of this redox step, the remaining major Q-band with much lower extinction coefficient exhibited λ_{max} close to the original Q_y band for **1a** and **1b** (639 nm) or to the original Q_z band for **4a** and **4b** (645 and 638 nm, respectively; see Figure 11, Table 4, and Supporting Information, Figure S7).

The Soret band for the TBTAP derivatives **4a** and **4b** remained mostly the same during the first oxidation process. In contrast, the tetrabenzoporphyrin derivatives **1a** and **1b** exhibited substantial diminished intensity of the Soret band, especially at 426 and 443 nm (**1a**) and 428 nm (**1b**); see Table 4 and Supporting Information, Figure S7. The most striking spectroscopic feature that results due to the second electrochemical oxidation process is the growth of a new peak between the Soret and Q-band regions with wavelength of peak maximums in the range of $467 \leq \lambda_{max} \leq 525$ nm for all four compounds, Figure 11 and Supporting Information, Figure S7. Formation of this new peak is accompanied by the near (ca. 80%) destruction of all absorptions in the Q-band region, and a further, much smaller (ca. 30%), lowering in intensity of the remaining Soret band absorptions.

4. CONCLUSIONS

An X-ray photoelectron spectroscopy study of the metal-free tetrabenzoporphyrin derivatives **1a** (only CH atom groups at the four meso positions), **2a** (one nitrogen atom and three CH atom groups at the four meso positions), **3a** (a nitrogen atom at each of two of the meso positions), and **4a** (nitrogen atoms at three of the four meso positions) revealed that it is possible to differentiate between all three types of nitrogen atoms in the structure. The binding energy of N_{meso} atoms (ca. 398.5 eV) is in between those of the inner core N (397.8 eV) and $\underline{N}H$ atoms (399.7 eV). Upon copper coordination, all three nitrogen-type peaks coalesce into one with binding energy ca. 398.2 eV. The UV−vis spectra of compounds of type **1**− **4** showed that Q-band peak maxima red shifts to longer wavelengths, and the Soret band peak maxima blue shifts to shorter wavelengths with increasing number of meso nitrogen atoms. Contemporaneously, the extinction coefficients of the Soret band decreased, while those of the Q-band increased. These changes could be related to the relative electron density on each macrocycle expressed as the sum of electronegativities of meso atom groups, $\sum\chi_R$. The electrochemical fingerprints of the compounds investigated consisted of two oxidative and two reductive redox steps in the potential window of the solvent (CH_2Cl_2) except for **1b** and **2b** where copper coordination

Table 4. UV–vis Spectral Data in CH_2Cl_2/0.1 mol dm^{-3} $[N(^nBu)_4][B(C_6H_5)_4]$ for the Most Dominant Peaks of 1 and 4 after Oxidation or Reduction; the Potential Range (vs Ag wire) at which the Spectral Changes Occurred Are also Recorded

compound	peak maximum λ_{max}, nm (ε/dm^3 mol^{-1} cm^{-1})[a]	E range, V[b]
1a^{2-}: M = 2H, 2nd reduction	443 (100 000); 455 (312 000); 657 (45 000)	−0.80 to −1.15
1a^{-}: M = 2H, 1st reduction	433 (209 000); 443, (137 000); 633 (78 000); 657 (36 000); 680 (28 000)	−0.55 to −0.75
1a: M = 2H, neutral	426 (204 000); 443 (275 000); 633 (64 000); 680 (52 000)	resting state
1a^{+}: M = 2H, 1st oxidation	426 (118 000); 443 (152 000); 639 (47 000); 682 (37 000)	0.00 to 0.30
1a^{2+}: M = 2H, 2nd oxidation	431 (54 000); 525 (26 000); 639 (46 000)	0.45 to 0.95
1b^{2-}: M = Cu, 2nd reduction	Redox process not observed in this solvent system	
1b^{-}: M = Cu, 1st reduction	429 (160 000); 640 (68 000); 663 (35 000)	−1.00 to −1.35
1b: M = Cu, neutral	430 (218 000); 638 (109 000); 661 (56 200)	resting state
1b^{+}: M = Cu, 1st oxidation	394 (80 100); 428 (66 000); 618 (52 000); 639 (61 000); 728 (21 000)	0.30 to 0.60
1b^{2+}: M = Cu, 2nd oxidation	394 (58 000); 428 (48 000); 497 (28 000); 639 (40 000)	0.85 to 1.35
4a^{2-}: M = 2H, 2nd reduction	418 (30 100); 645 (31 900); 708 (17 200)	−0.95 to −1.40
4a^{-}: M = 2H, 1st reduction	365 (36 200); 406 (37 400); 418 (49 300); 645 (42 000); 708 (66 100)	−0.50 to −0.85
4a: M = 2H, neutral	361 (56 200); 406 (46 800); 644 (45 200); 675 (78 300); 716 (123 000)	resting state
4a^{+}: M = 2H, 1st oxidation	363 (62 100); 406 (38 000); 645 (47 300); 677 (41 900); 716 (35 800)	0.00 to 0.60
4a^{2+}: M = 2H, 2nd oxidation	316 (69 700); 363 (45 400); 467 (40 100) 644 (16 700)	0.60 to 1.00
4b^{2-}: M = Cu, 2nd reduction	359 (23 200), 571 (16 100), 632 (17 900) 708 (10 700)	−0.95 to −1.40
4b^{-}: M = Cu, 1st reduction	359 (32 900), 395 (29 000), 638 (24 100), 676 (37 800), 702 (50 100)	−0.55 to −0.85
4b: M = Cu, neutral	361 (47 800), 395 (47 800), 638 (46 400), 676 (89 400), 700 (128 800)	resting state
4b^{+}: M = Cu, 1st oxidation	340 (70 000), 638 (60 700), 678 (54 100)	0.35 to 0.60
4b^{2+}: M = Cu, 2nd oxidation	340 (51 700), 482 (40 300), 638 (21 100)	0.85 to 1.35

[a] Resting (neutral) state ε values are as per Table 1, but due to the continuous scanning of potential while recording UV–vis spectra, precision for the reduced or oxidized species is only to three significant figures. [b] Applied potential ranges to the OTTLE cell to cause the observed spectroscopic changes. Applied potentials differ from Table 3 because the OTTLE cell potentials are referenced in situ to a silver wire.

caused the second reductive redox step to move outside the negative potential limit of the solvent. Computational chemical methods using DFT confirmed **1b** to involve a Cu(II) reduction prior to ring-based reductions. In addition, DFT calculations showed that for **2b**, Cu(II) reduction as the first reductive step is only feasible if the nonperipheral substituents R are hydrogen. However, when R = Me it becomes the second reduction process; when R is ethyl, propyl, or hexyl it becomes the third reductive process. Again, redox potentials for all four redox processes can be related to the relative electron density on each macrocycle, $\sum\chi_{R}$. However, the electrochemically determined HOMO–LUMO gap, [$E^{o\prime}$(first anodic process) − $E^{o\prime}$(first cathodic process)] could not be linearly related to λ_{max} of the Q-bands, thereby indicating the value of Q-band λ_{max} is not uniquely governed by the simple one-orbital treatment of electrochemically determined HOMO–LUMO gaps.

■ ASSOCIATED CONTENT

Ⓢ Supporting Information

Frontier molecular orbitals of **1b**–**5b**; an energy level diagram of **1b** with a table presenting numerical data; relationship between experimental $E^{o\prime}$ and calculated HOMO or LUMO energy levels; multiple scan rate CVs, LSVs, and SWs of **1a** and **1b**; the relationship between Q-band λ_{max} values and $\Delta E^{o\prime} = E^{o\prime}_{\text{wave 1}} - E^{o\prime}_{\text{wave 3}}$; UV–vis spectra generated during spectroelectrochemical experiments; optimized Cartesian coordinates for compounds. The Supporting Information is available free of charge on the ACS Publications website at DOI: 10.1021/acs.inorgchem.5b00380.

■ AUTHOR INFORMATION

Corresponding Author

*Fax: +27 51 4017295. E-mail address: swartsjc@ufs.ac.za.

Notes

The authors declare no competing financial interest.

■ ACKNOWLEDGMENTS

J.C.S. acknowledges the NRF under Grant No. 2054243 and the UFS for financial support. M.J.C. acknowledges the award of an Emeritus Fellowship from the Leverhulme Trust.

■ REFERENCES

(1) (a) *Handbook of Porphyrin Science;* Kadish, K. M., Smith, K. M., Guilard, R., Eds.; World Scientific Publishing: Singapore, 2010–2012; Vols. *1*–*20*, and references therein. (b) *The Porphyrin Handbook;* Kadish, K. M, Smith, K. M., Guilard, R. Eds. Academic Press: Waltham, MA, 2000–2003; Vols. *1*–*20*, and references therein. (c) Mack, J.; Kobayashi, N. *Chem. Rev.* **2011**, *111*, 281–321. (d) Urbani, M.; Grätzel, M.; Nazeeruddin, M. K.; Torres, T. *Chem. Rev.* **2014**, *114*, 2192–2277.

(2) Hanabusa, K.; Shirai, H. In *Phthalocyanines: Properties and Applications;* Leznoff, C. C., Lever, A. B. P., Eds.; VCH Publishers: New York, 1993; Vol. 2, Ch. 5, pp 197–222.

(3) (a) Gregory, P. *High-Technology Applications of Organic Colorants;* Plenum Press: New York, 1991. (b) Gregory, P. *J. Porphyrins Phthalocyanines* **2000**, *4*, 432–437.

(4) Shima, T.; Yamakawa, Y.; Nakano, T.; Kim, J.; Tominaga, J. *Japan. J. Appl. Phys., Part 2* **2006**, *45*, L1007–L1009.

(5) Mustroph, H.; Stollenwerk, M.; Bressau, V. *Angew. Chem., Int. Ed.* **2006**, *45*, 2016–2035.

(6) Zhou, R.; Josse, F.; Gopel, W.; Ozturk, Z. Z.; Bekaroglu, O. *Appl. Organomet. Chem.* **1996**, *10*, 557–577.

(7) Ogura, S.; Tabata, K.; Fukushima, K.; Kamachi, T.; Okura, I. *J. Porphyrins Phthalocyanines* **2006**, *10*, 1116–1124.

(8) (a) Piechocki, C.; Simon, J.; Skoulious, A.; Guillon, D.; Weber, J. P. *J. Am. Chem. Soc.* **1982**, *104*, 5245–5247. (b) Cherodian, A. S.; Davies, A. N.; Richardson, R. M.; Cook, M. J.; McKeown, N. B.; Thomson, A. T.; Feijoo, J.; Ungar, G.; Harrison, K. J. *Mol. Cryst. Liq. Cryst.* **1991**, *196*, 103–114. (c) Cook, K. J.; Cracknell, S. J.; Harrison, K. J. *J. Mater. Chem.* **1991**, *1*, 703–704. (e) Cammidge, A. N.; Chambrier, I.; Cook, M. J.; Langner, E. H. G.; Rahman, M.; Swarts, J. C. *J. Porphyrins Phthalocyanines* **2011**, *15*, 890–897.

(9) (a) Mukherjee, B.; Ray, A. K.; Sharma, A. K.; Cook, M. J.; Chambrier, I. *J. Appl. Phys.***2008**, *103*, Article No. 074507. (b) Majumdar, H. S.; Bandyopadhyay, A.; Pal, A. J. *Org. Electron.* **2003**, *4*, 39–44.

(10) (a) O'Flaherty, S. M.; Hold, S. V.; Cook, M. J.; Torres, T.; Chen, Y.; Hanack, M.; Blau, W. J. *Adv. Mater.* **2003**, *15*, 19–32. (b) Auger, A.; Blau, W. J.; Burnham, P. M.; Chambrier, I.; Cook, M. J.;

Isare, B.; Nekelson, F.; O'Flaherty, S. M. *J. Mater. Chem.* **2003**, *13*, 1042−1047.

(11) Wöhrle, D.; Suvorova, O.; Gerdes, R.; Bartels, R.; Lapok, L.; Baziakina, N.; Makarov, S.; Slodek, A. *J. Porphyrins Phthalocyanines* **2004**, *8*, 1020−1041.

(12) (a) Li, R.; Zhang, X.; Zhu, P.; Ng, D. K. P.; Kobayashi, N.; Jiang, J. *Inorg. Chem.* **2006**, *45*, 2327−2334. (b) Cook, M. J.; Chambrier, I.; Cracknell, S. J.; Mayes, D. A.; Russell, D. A. *Photochem. Photobiol.* **1995**, *62*, 542−545.

(13) (a) Swarts, J. C.; Langner, E. H. G.; Krokeide-Hove, N.; Cook, M. J. *J. Mater. Chem.* **2001**, *11*, 434−443. (b) Ou, Z.; Zhan, R.; Tomachynski, L. A.; Chernii, V. Ya.; Kadish, K. M. *Macroheterocycles* **2011**, *4*, 164−170.

(14) (a) Chambrier, I.; Swarts, J. C.; Hughes, D. L.; Cook, M. J. *J. Porphyrins Phthalocyanines* **2009**, *13*, 175−187. (b) Louati, A.; El Meray, M.; Andre, J. J.; Simon, J.; Kadish, K. M.; Gross, M.; Giraudeau, A. *Inorg. Chem.* **1985**, *24*, 1175−1179. (c) Nevin, W. A.; Hempstead, M. R.; Liu, W.; Leznoff, C. C.; Lever, A. B. P. *Inorg. Chem.* **1987**, *26*, 570−577.

(15) (a) Cook, M. J.; Chambrier, I.; White, G. F.; Fourie, E.; Swarts, J. C. *Dalton Trans.* **2009**, 1136−1144. (b) Chambrier, I.; Hughes, D. L.; Swarts, J. C.; Isare, B.; Cook, M. J. *Chem. Commun.* **2006**, 3504−3506. (c) Giraudeau, A.; Louati, A.; Gross, M.; Andre, J. J.; Simon, J.; Su, C. H.; Kadish, K. M. *J. Am. Chem. Soc.* **1983**, *105*, 2917−2919.

(16) (a) Weschler, C. J.; Hoffmann, B. M.; Basolo, F. *J. Am. Chem. Soc.* **1975**, *97*, 5278−5280. (b) Jameson, G. B.; Ibers, J. A. In *Bioinorganic Chemistry;* Bertini, I.; Gray, H. B., Lippard, S. J., Valentine, J. S., Eds.; University Science Books: Mill Valley, CA, 1994; Ch. 4, pp 167−252.

(17) (a) De Silva, D. G. A. H.; Powls, R.; Sykes, A. G. *Biochim. Biophys. Acta* **1988**, *933*, 460−469. (b) Grey, H. B.; Ellis, W. R. In *Bioinorganic Chemistry;* Bertini, I., Gray, H. B., Lippard, S. J., Valentine, J. S., Eds.; University Science Books: Mill Valley, CA, 1994; Ch. 6, pp 315− 363.

(18) (a) Conradie, J.; Swarts, J. C.; Ghosh, A. *J. Phys. Chem. B* **2004**, *108*, 452−456. (b) Hansen, T.; Ovesen, H.; Svadberg, A.; Svendsen, K.; Tangen, E.; Swarts, J. C.; Ghosh, A. *Organometallics* **2004**, *23*, 3870−3872.

(19) (a) Kostas, I. D.; Coutsolelos, A. G.; Charalambidis, G.; Skondra, A. *Tetrahedron Lett.* **2007**, *48*, 6688−6691. (b) Monnereau, C.; Ramos, P. H.; Deutman, A. B. C.; Elemans, J. A. A. W.; Nolte, R. J. M.; Rowan, A. E. *J. Am. Chem. Soc.* **2010**, *132*, 1529−1531.

(20) Ethirajan, M.; Chen, Y.; Joshi, P.; Pandey, R. K. *Chem. Soc. Rev.* **2011**, *40*, 340−362.

(21) (a) Auger, A.; Muller, A. J.; Swarts, J. C. *Dalton Trans.* **2007**, 3623−3633. (b) Auger, A.; Swarts, J. C. *Organometallics* **2007**, *26*, 102−109.

(22) (a) Carvalho, C. M. B.; Brocksom, T. J.; de Oliviera, K. T. *Chem. Soc. Rev.* **2013**, *42*, 3302−3317. (b) Okujima, T.; Hashimoto, Y.; Jin, G.; Yamada, H.; Ono, N. *Heterocycles* **2009**, *77*, 1235−1248. (c) Claessens, C. G.; González-Rodríguez, D.; Rodríguez-Morgade, M. S.; Medina, A.; Torres, T. *Chem. Rev.* **2014**, *114*, 2192−2277. (d) Fukuda, T.; Kobayashi, N. *Dalton Trans.* **2008**, 4685−4704.

(23) Cammidge, A. N.; Chambrier, I.; Cook, M. J.; Sosa-Vargas, L. In *Handbook of Porphyrin Science;* Kadish, K. M., Smith, K. M., Guilard, R., Eds.; World Scientific: Singapore, 2012; Vol. *16*, pp 331−404.

(24) (a) Tse, Y.-H; Goel, A.; Hu, M.; Lever, A. B. P.; Leznoff, C. C.; Van Lier, J. E. *Can. J. Chem.* **1993**, *71*, 742−753. (b) Fu, Y.; Forman, M.; Leznoff, C. C.; Lever, A. B. P. *J. Phys. Chem.* **1994**, *98*, 8985−8991.

(25) Khene, S.; Cammidge, A. N.; Cook, M. J.; Nyokong, T. *J. Porphyrins Phthalocyanines* **2007**, *11*, 761−770.

(26) Mack, J.; Sosa-Vargas, L.; Coles, S. J.; Tizzard, G. J.; Chambrier, I.; Cammidge, A. N.; Cook, M. J.; Kobayashi, N. *Inorg. Chem.* **2012**, *51*, 12820−12833.

(27) Cammidge, A. N.; Chambrier, I.; Cook, M. J.; Hughes, D. L.; Rahman, M.; Sosa-Vargas, L. *Chem.—Eur. J.* **2011**, *17*, 3136−3146.

(28) LeSuer, R. J.; Buttolph, C.; Geiger, W. E. *Anal. Chem.* **2004**, *76*, 6395−6401.

(29) Moulder, F.; Stickle, W. F.; Sobol, P. E.; Bomben, K. D. *Handbook of X-ray Photo-electron Spectroscopy;* ULVAC-PHI, Inc: Chigasaki, Japan, 1995; pp 45, 57, 143.

(30) (a) Gritzner, G.; Kuta, J. *Pure Appl. Chem.* **1984**, *56*, 461−466. (b) Gagne, R. R.; Koval, C. A.; Lisensky, G. C. *Inorg. Chem.* **1980**, *19*, 2855−2857.

(31) (f) The potential of ferrocene versus SCE was reported as 0.425 V in CH$_3$CN and 0.450 V in CH$_2$Cl$_2$, see Lever, A. B. P.; Milaeva,E. R.; Speier, G. In *Phthalocyanines, Properties and Applications;* Leznoff, C. C., Lever, A. B. P., Eds.; VCH Publishers, Inc.: New York, 1993; Ch.1, p 8. Leading references describing the electrochemical activity and behaviour of ferrocene and decamethylferrocene in a multitude of organic solvents are (a) Noviandri, I.; Brown, K. N.; Fleming, D. S.; Gulyas, P. T.; Lay, P. A.; Masters, A. F.; Phillips, L. *J. Phys. Chem. B* **1999**, *103*, 6713−6722. (b) Connelly, N. G.; Geiger, W. E. *Chem. Rev.* **1996**, *96*, 877−910. (c) Ruiz, J.; Astruc, D. *C. R. Acad. Sci., Ser. IIc: Chim.* **1998**, *1*, 21−27. (d) Aranzaes, R. J.; Daniel, M. C.; Astruc, D. *Can. J. Chem.* **2006**, *84*, 288−299. (e) Fourie, E.; Swarts, J. C.; Chambrier, I.; Cook, M. J. *Dalton Trans.* **2009**, 1145−1154.

(32) Krejčik, M.; Daněk, M.; Hartl, F. *J. Electroanal. Chem.* **1991**, *317*, 179−187.

(33) Becke, A. D. *Phys. Rev. A* **1988**, *38*, 3098−3100.

(34) Lee, C. T.; Yang, W. T.; Parr, R. G. *Phys. Rev. B* **1988**, *37*, 785−789.

(35) Frisch, M. J.; Trucks, G. W.; Schlegel, H. B.; Scuseria, G. E.; Robb, M. A.; Cheeseman, J. R.; Scalmani, G.; Barone, V.; Mennucci, B.; Petersson, G. A.; Nakatsuji, H.; Caricato, M.; Li, X.; Hratchian, H. P.; Izmaylov, A. F.; Bloino, J.; Zheng, G.; Sonnenberg, J. L.; Hada, M.; Ehara, M.; Toyota, K.; Fukuda, R.; Hasegawa, J.; Ishida, M.; Nakajima, T.; Honda, Y.; Kitao, O.; Nakai, H.; Vreven, T.; Montgomery, J. A., Jr.; Peralta, J. E.; Ogliaro, F.; Bearpark, M.; Heyd, J. J.; Brothers, E.; Kudin, K. N.; Staroverov, V. N.; Keith, T.; Kobayashi, R.; Normand, J.; Raghavachari, K.; Rendell, A.; Burant, J. C.; Iyengar, S. S.; Tomasi, J.; Cossi, M.; Rega, N.; Millam, J. M.; Klene, M.; Knox, J. E.; Cross, J. B.; Bakken, V.; Adamo, C.; Jaramillo, J.; Gomperts, R.; Stratmann, R. E.; Yazyev, O.; Austin, A. J.; Cammi, R.; Pomelli, C.; Ochterski, J. W.; Martin, R. L.; Morokuma, K.; Zakrzewski, V. G.; Voth, G. A.; Salvador, P.; Dannenberg, J. J.; Dapprich, S.; Daniels, A. D.; Farkas, O.; Foresman, J. B.; Ortiz, J. V.; Cioslowski, J.; Fox, D. J. *Gaussian 09*, Revision C.01; Gaussian Inc.: Wallingford, CT, 2010.

(36) Josefsen, L. B.; Boyle, R. W. *Met.-Based Drugs* **2008**; DOI 10.1155/2008/276109, 24 pages.

(37) (a) Yamashige, H.; Shuiji, M.; Tsutomu, K.; Perera, R. C.; Hisanobu, W. *Anal. Sci.* **2005**, *21*, 635−639. (b) Polzonetti, G.; Carravetta, V.; Iucci, G.; Ferri, A.; Paolucci, G.; Goldoni, A.; Parent, P.; Laffon, C.; Russo, M. V. *Chem. Phys.* **2004**, *296*, 87−100. (c) Alfredsson, Y.; Brena, B.; Nilson, K.; Ahlind, J. *J. Chem. Phys.* **2005**, *122*, Article No. 214723. (d) Zhao, P.; Niu, L.; Huang, L.; Zhang, F. *J. Electrochem. Soc.* **2008**, *155*, C515−C520.

(38) Adolphi, B.; Berger, O.; Fischer, W. J. *Appl. Surf. Sci.* **2001**, *179*, 102−108.

(39) (a) Lever, A. B. P.; Milaeva, E. R.; Speier, G. *Phthalocyanines - Properties and Applications;* Leznoff, C. C, Lever, A. B. P, Eds.; VCH: New York, 1993; Vol. 3, pp 1. (b) Ahmida, M. M.; Eichhorn, S. H. *ECS Trans.* **2010**, *25*, 1−10.

(40) Nemykin, V. N.; Galloni, P.; Floris, B.; Barrett, C. D.; Hadt, R. G.; Subbotin, R. I.; Marrani, A. G.; Zanoni, R.; Loim, N. M. *Dalton Trans.* **2008**, 4233−4246.

(41) (a) Shao, J.; Zhao, H.; Ohkubo, K.; Wasbotten, I. H.; Fukuzumi, S.; Ghosh, A.; Kadish, K. M. *J. Porphyrins Phthalocyanines* **2004**, *8*, 1236−1247. (b) Thomas, K. E.; Alemayehu, A. B.; Conradie, J.; Beavers, C.; Ghosh, A. *Inorg. Chem.* **2011**, *50*, 12844−12851.

(42) (a) Kuhn, A.; von Eschwege, K. G.; Conradie, J. *J. Phys. Org. Chem.* **2012**, *25*, 58−68. (b) Kuhn, A.; von Eschwege, K. G.; Conradie, J. *Electrochim. Acta* **2011**, *56*, 6211−6218. (c) Conradie, J. *Electrochim. Acta* **2013**, *110*, 718−725. (d) Landman, M.; Pretorius, R.; Fraser, R.; Buitendach, B. E.; Conradie, M. M.; van Rooyen, P. H.; Conradie, J. *Electrochim. Acta* **2014**, *130*, 104−118.

(43) (a) Swarts, J. C.; Nafady, A.; Roudebush, J. H.; Trupia, S.; Geiger, W. E. *Inorg. Chem.* **2009**, *48*, 2156−2165. (b) Barriere, F.; Kirss, R. U.; Geiger, W. E. *Organometallics* **2005**, *24*, 48−52. (c) Kemp, K. C.; Fourie, E.; Conradie, J.; Swarts, J. C. *Organometallics* **2008**, *27*, 353−362. (d) Nafady, A.; Chin, T. T.; Geiger, W. E. *Organometallics* **2006**, *25*, 1654−1663. (e) Chong, D. S.; Slote, J.; Geiger, W. E. *J. Electroanal. Chem.* **2009**, *630*, 28−34. (f) F. Barriere, F.; Geiger, W. E. *J. Am. Chem. Soc.* **2006**, *128*, 3980−3989. (g) Ziegler, C. J.; Chanawanno, K.; Hasheminsasab, A.; Zatsikha, Y. V.; Maligaspe, E.; Nemykin, V. N. *Inorg. Chem.* **2013**, *53*, 4751−4755.

(44) (a) Evans, D. H.; O'Connell, K. M.; Peterson, R. A.; Kelly, M. J. *J. Chem. Educ.* **1983**, *60*, 290−293. (b) Gericke, H. J.; Barnard, N. I.; Erasmus, E.; Swarts, J. C.; Cook, M. J.; Aquino, M. A. S. *Inorg. Chim. Acta* **2010**, *363*, 2222−2232. (c) Kissinger, P. T.; Heineman, W. R. *J. Chem. Educ.* **1983**, *60*, 702−706. (d) Van Benshoten, J. J.; Lewis, J. Y.; Heineman, W. R.; Roston, D. A.; Kissinger, P. T. *J. Chem. Educ.* **1983**, *60*, 772−776. (e) Mobbott, G. A. *J. Chem. Educ.* **1983**, *60*, 697−702.

(45) (a) Quinton, D.; Antunes, E.; Griveau, S.; Nyokong, T.; Bedioui, F. *Inorg. Chem. Commun.* **2011**, *14*, 330−332. (b) Nemykin, V. N.; Rohde, G. T.; Barrett, C. D.; Hadt, R. G.; Bizzarri, C.; Galloni, P.; Floris, B.; Nowik, I.; Herber, R. H.; Marrani, A. G.; Zanoni, R.; Loim, N. M. *J. Am. Chem. Soc.* **2009**, *131*, 14969−14978.